



Water, CO₂ and Argon Permeabilities of Intact and Fractured Shale Cores Under Stress

Reinier van Noort¹ · Viktoriya Yarushina¹

Received: 4 July 2018 / Accepted: 24 September 2018 / Published online: 28 September 2018
© The Author(s) 2018

Abstract

As shale is the caprock over many reservoirs targeted for CO₂ storage, shale permeability to CO₂ has become an important concern. Measurements of this permeability need to be performed under in-situ conditions, with realistic temperatures, confining pressures and fluid pressures, and the effects of variables such as pressure, temperature, and shale moisture content need to be thoroughly addressed. Furthermore, the exposure of wet shale to dry CO₂ can lead to, for example, dehydration and two-phase flow, that in turn affect permeability. This paper reports shale permeability measurements performed on two shale core plugs from Svalbard, under in-situ pressure and temperature conditions relevant for CO₂ storage, using argon, CO₂, and water as the permeate, and using both transient pulse and constant flow techniques. Permeability was found to be dependent mainly on effective confining pressure and on shale moisture content. The following was observed: (1) permeability decreased with increasing effective confining pressure; (2) permeability to water was lower than permeability to Ar or CO₂; (3) shale moisture content had a strong inhibiting effect on the flow of Ar and CO₂; (4) when a high CO₂-flow was applied to a shale sample containing a hydrous pore fluid, a breakthrough effect occurred; and (5) in the presence of pore water, compaction creep can occur, causing a permanent decrease in permeability.

Keywords CO₂ storage · Caprock · Shale · Permeability · Fluid flow

1 Introduction

Argillaceous rocks, such as shale, are an important component in a wide range of geo-engineering systems. In petroleum systems, shale can be a source rock, reservoir rock, seal, or all simultaneously. In geological carbon capture and storage (CCS), shale is a common caprock over targeted reservoirs. In nuclear waste disposal, argillaceous rocks have been considered as hosts for geological disposal facilities (e.g., Delage et al. 2010). The importance of shale as a caprock or seal is related to its low porosity, very low permeability, and its ability to deform in a ductile manner, effectively relaxing high stresses. However, the exact role played by shales in sub-surface fluid flow systems remains enigmatic. While their low permeability is supposed to effectively eliminate any fluid flow across shaley layers, evidence for cross-layer (vertical) fluid communication between

reservoirs separated by thick shale layers has been reported (e.g., Huq et al. 2017). Furthermore, hydrocarbons generated within shales during the maturation of organic matter can successfully be expelled into surrounding rocks. A proper assessment of the (long-term) environmental safety of CO₂ and nuclear waste storage as well as successful hydrocarbon production, therefore, requires a good understanding of fluid flow processes through shales.

Accordingly, in recent years, renewed focus has been directed at performing permeability and fluid flow measurements on shales (e.g., Hildenbrand et al. 2002, 2004; Dong et al. 2010; Chalmers et al. 2012; Chalmers and Bustin 2012; Skurtveit et al. 2012; Ghanizadeh et al. 2014, 2015; Heller et al. 2014; Gutierrez et al. 2015; Zhang et al. 2015, 2016a; Van Noort and Yarushina 2016; Makhnenko et al. 2017; Tian et al. 2017). Despite these efforts, the mechanism or mechanisms by which fluid flows through low-permeable shales under effective confinement remains an unresolved issue, especially when dealing with the flow of one fluid, such as CO₂ or Ar, through a shale containing another, hydrous (wetting) pore fluid. Furthermore, shale permeability shows a strong dependence on current effective confinement, and

✉ Reinier van Noort
Reinier@ife.no

¹ Department of Environmental Analysis, Institute for Energy Technology, Postbox 40, 2027 Kjeller, Norway

may also depend on stress history. Accurate measurements of mechanical properties of shale have shown that, even at low pressures, shales deform not only elastically and plastically, but also by time-dependent viscous deformation (Chang and Zoback 2009; Brantut et al. 2013; Sone and Zoback 2014; Räss et al. 2017). In turn, this deformation influences permeability (e.g., Chhatre et al. 2014; Gutierrez et al. 2015).

In addition to pores, planar features such as (micro)fractures may play an important role in (macroscopic) fluid flow processes through low-porosity/low-permeability rocks such as shale. However, the exact role of such fractures remains unclear. While some studies report flow through fractures as the main transport mechanism (e.g., Gutierrez et al. 2000), this is much more expected in dried laboratory samples or a freshly stimulated unconventional reservoir rather than in clay-rich water-saturated shales present at greater depths. Furthermore, shale permeability and the active fluid flow mechanism may also depend on the fluid type used (e.g., Ghanizadeh et al. 2014; Van Noort and Yarushina 2016), for example, due to differences in surface tension between different fluids (Rozhko 2016), and water adsorption at mineral surfaces (Ghanizadeh et al. 2014). Shale wettability controls the capillary entry pressure and the flow path geometry within partially saturated rock (e.g., Borysenko et al. 2009), and in turn, both the average pore size and the pore-size distribution may influence shale permeability (Tian et al. 2017). Ilton et al. (2012) and Schaef et al. (2012) hypothesize that the dehydration of swelling clays due to exposure to dry supercritical CO₂ can result in an increase in permeability. In contrast, Busch et al. (2016) expect such effects to be negligible, as dehydration will be limited to the shale volume directly around the wellbores through which CO₂ is injected. It could, however, be expected that this zone expands as long as CO₂ injection continues, with the expansion rate dependent on (layer parallel) shale permeability. Furthermore, as wells are one of the main leakage risks, drying and shrinkage around these wells could be particularly problematic for maintaining well integrity. The dissolution and precipitation of reactive minerals may potentially cause changes in permeability (Armitage et al. 2013), though Bateman et al. (2013) reported no significant effects for the Utsira shale. Finally, shale permeability may also be affected by fines migration (Borchardt et al. 1984), causing clogging or re-opening of pore throats.

Recent experimental studies on CO₂ injection into wet shales and other clay-rich materials reported the formation of localized fluid flow pathways (Harrington et al. 2012; Skurtveit et al. 2012; Wiseall et al. 2015). These narrow pathways were accompanied by dilation, and they were transient and closed again once the pore pressure dropped as a result of flow. It was hypothesized that these breakthrough events that were induced during injection were related to

changes in pore wetting and/or effective confinement resulting from increases in fluid pressure. However, the exact mechanisms by which these events occur are not yet fully understood.

Theoretical studies predict that time-dependent deformation of shales, combined with their pressure-sensitive permeability, may lead to fluid flow focusing effects that do not require pre-existing fractures (Räss et al. 2014; Yarushina and Podladchikov 2015; Yarushina et al. 2015), causing the formation of thin channels which, in shales, have diameters on the order of μm to mm. Such micro-channels can cut through shaley layers that are otherwise assumed to be impermeable flow barriers. Therefore, properly understanding the flow of fluids through shale, as well as the possible interactions between shale and fluid that may influence this flow, such as mechanical effects (Yarushina and Podladchikov 2015), chemical reactions (Credoz et al. 2009; Alemu et al. 2011), and swelling or shrinkage of clay minerals (Ilton et al. 2012; Schaef et al. 2012; De Jong et al. 2014), especially under conditions relevant for the storage of CO₂, is of great importance. This requires the accurate experimental quantification of shale permeability and viscoelastoplasticity under stress, and the incorporation of such measurements into numerical models of fluid flow coupled with geomechanics.

With this in mind, we investigated the effects of varying permeating fluid, effective confining pressure, and transient creep on matrix and fracture permeability of early Cretaceous shale samples. We performed 180 transient pulse permeability measurements and 12 constant flow permeability measurements on two core plugs from the Rurikfjellet formation in Svalbard. Permeability measurements were conducted using water, liquid, and supercritical CO₂, and argon (Ar) as pore fluids, at effective pressures ranging from 1.4 to 37.4 MPa. One of the shale core plugs studied split between measurements, and further measurements were performed on the fractured plug, allowing us to compare the permeability of a fractured sample to that of the same sample when unfractured. Our measurements provide insights into the permeability of the Rurikfjellet shale, and into the role of water and confining pressure in controlling the flow of CO₂ and other fluids through shales. In this paper, we will discuss our measurements and their implications.

2 Method

2.1 Samples

In this work, we used two core plugs, drilled from a single core, at the same horizon and less than 3 cm apart to ensure that there were no significant differences in mineralogy or microstructure between the two samples. The core used was

retrieved on 23 June 2012 from borehole DH7A at the Longyearbyen CO₂ well park in Adventdalen, on Svalbard's main island Spitsbergen on the northwestern margin of the Barents Sea Shelf (Braathen et al. 2012; Huq et al. 2017). This specific core section originated from the Rurikfjellet formation, and was retrieved from a depth of 375.25 to 375.47 m. XRD analyses showed that the main mineral phases present in our sample are quartz (~55–60%), illite with minor interlayered smectite (20–25%), and chlorite (~10%). Minor phases identified are kaolinite, plagioclase. Some larger (mm-sized) grains of pyrite were observed in the samples optically. The selected shale was homogeneously gray in color, with a very fine (sub-mm scale), parallel bedding. There was no clear compositional variation across the bedding, with no visible differences between individual layers. Both plugs used in this study were drilled dry while keeping the shale under physical compression to prevent fracturing. The plugs were drilled parallel to the bedding direction, and had a diameter of 25 mm and a thickness of 10 mm.

Several series of measurements were performed on each sample, with conditions (temperature, pressure, and/or fluid used) changing between individual measurement series. After the first series of measurements performed

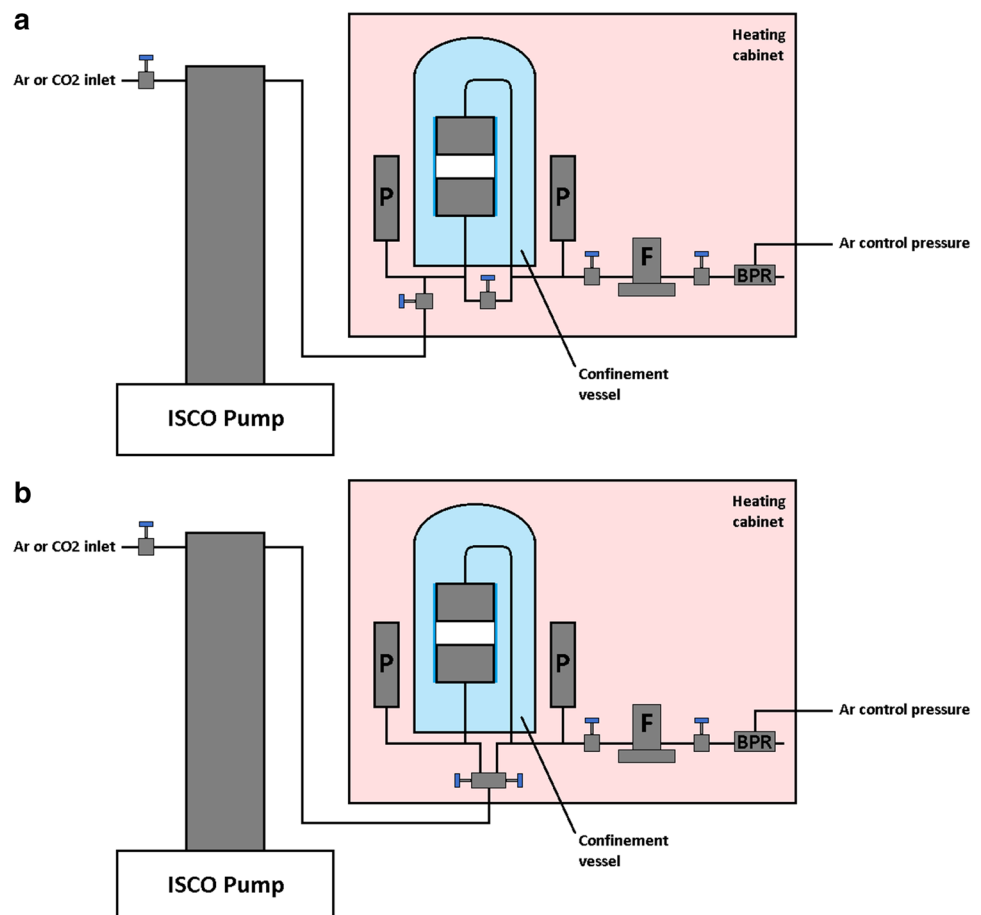
on Sample 1, this plug split parallel to its bedding during a jacket replacement. The fractured sample was carefully reinserted into the apparatus, and further measurements were performed on it in that state.

2.2 Apparatus and Method

All measurements reported here were carried out in a purpose-built permeability apparatus. After measurements on Sample 1 were completed, the apparatus was partly rebuilt, mainly to improve ease of use; apparatus performance was not otherwise affected. Schematic drawings of the original and modified apparatus are presented in Fig. 1. With our apparatus, transient pulse as well as constant flow-type permeability measurements can be performed interchangeably. Whereas the up- and downstream volumes in the configuration used for transient pulse measurements in the original apparatus were quite different (4.84 and 12.71 ml, respectively), in the current configuration, these volumes are near-identical (5.04 and 5.67 ml).

When preparing the shale sample plug for measurements, it was first sandwiched between two hastelloy porous frits (to act as flow and pressure distributors), and in turn placed

Fig. 1 Permeability apparatus, **a** as it was used during the measurements on Sample 1 and **b** upgraded version used for all later measurements



between two hastelloy pistons with grooved top surfaces and a central bore. Next, this assembly was jacketed in heat-shrink FEP, which was further sealed with steel wire tourniquets over grooves in the piston walls. The sample–piston–jacket assembly was then built into the apparatus. The confining pressure and pore fluid pressure were subsequently applied in alternating steps (using water as the confining medium), ensuring that the maximum effective confining pressure ($P_{\text{eff}} = P_c - P_f$) always stayed below the value at which measurements were to be made.

When the pore fluid was replaced between measurement series, the confining pressure and pore fluid were released in alternating steps. Once the pore fluid pressure was fully released, the pore fluid system was repeatedly vacuumized and flooded with the replacing fluid, to ensure purity. Next, the confining and pore pressures were raised once more in alternating steps. Most measurements on Sample 1 were performed using demineralized water. Before the CO₂ measurements on Sample 1, this sample was repeatedly flushed with supercritical CO₂, and then air-dried (inside its jacket assembly but outside the apparatus) in an attempt to remove its pore water. Initial measurements on Sample 2 were performed using Ar and CO₂. The fifth series of measurements was performed using distilled water. After this series, when this water was replaced with CO₂, the sample was vacuumized and flooded with CO₂ repeatedly, and was also flushed with CO₂ from the upstream side twice to remove as much water as possible while keeping the sample contained in the vessel. Demineralized or distilled water was used here, because the original pore fluid composition was not known, and only minor amounts of swelling clays were present in our samples.

Once the sample had stabilized under its confinement, transient pulse permeability measurements were performed by starting the data logger (typically logging at 1 Hz), closing the up- and downstream valves, raising the pump pressure to achieve the desired pulse pressure, and then briefly opening the upstream valve to apply the pressure pulse (either ~0.2 or ~0.5 MPa). By logging both the up- and downstream pressure, the decay of the pressure pulse was recorded. The permeability was subsequently calculated from this pulse decay.

Constant flow permeability measurements were performed by applying a constant volumetric flow into the sample via the ISCO pump. The induced flow through the sample was then measured directly using a Bronkhorst M13 CORI-FLOW mass flow meter placed downstream, while the downstream pressure was controlled by an Equilibar Zero Flow back-pressure regulator, designed to operate with very low flowrates. Changing from transient pulse to constant flow measurements did not require any changes to our apparatus or depressurization of the sample. To initiate a constant flow measurement, first data logging was started.

Next, the flowmeter was calibrated at zero flow and the correct downstream pressure by closing the valves on either side of the flowmeter. Once the flowmeter zero point was calibrated correctly, these valves were opened again, the valve connecting the downstream system to the pump was closed, and the desired flow rate was set on the ISCO pump, starting the measurement. Typically, a measurement would run until a constant mass flow, and up- and downstream pressure were reached, so that the pressure difference at that flowrate could be used to calculate sample permeability.

2.3 Data Treatment

Except when permeabilities were high, so that pressure changes were rapid, all up- and downstream pressure data sets were first smoothed using a variable moving average routine to reduce noise. Typically, this smoothing was done over a pressure change of 5 kPa (1.0% or 2.5% of the applied pressure pulse). Next, volumetric flow rates through the sample (Q) were calculated from the measured pressure and temperature data, based on fluid densities obtained using the FLUIDCAL software (Wagner 2014). From these flowrates, the permeability (k) was then calculated using Darcy's law:

$$-k = \frac{Q\mu l}{A(P_U - P_D)}, \quad (1)$$

where μ is the dynamic viscosity (also obtained using the FLUIDCAL software of Wagner 2014), l is the sample length, and A is the sample surface area through which flow takes place. P_U and P_D are the up- and downstream pressures, respectively. Using this equation, permeabilities were calculated for each data point over a set change in pressure around that data point to smoothen out noise effects in the data. Typically, this pressure step was 10 or 20 kPa—4–5% of the total pressure differential pulse applied to the sample. Using a sufficiently small pressure step over which to treat our data, a near-constant flow over each increment was ensured. Any measurements in which a leakage on the system was suspected were disregarded. Note that this approach neglects compressive storage effects in the sample. However, considering the relatively small pressure step used and small pore volume compared to our system volume, these effects could be considered negligible.

Constant flow permeabilities were calculated from the measured mass flowrates, and up- and downstream pressures, also using Darcy's law. First, the measured mass flowrates were corrected for any remaining zero-point offset of the flowmeter. Next, the permeability was calculated for the averaged measured (i.e., downstream) flowrate and up- and downstream pressures over the segment of data, where stable flow was achieved.

3 Results

3.1 Permeability Measurements

Figure 2 gives an example of the raw pressure data measured during a transient pulse test. We have performed five series of measurements on Sample 1, using a transient pulse technique (see Table 1; Fig. 3). This sample was initially intact but split along its bedding after the first series of measurements. Series 1–4 were performed using water as the pore fluid, while series 5 was performed using supercritical CO₂. Series 1 and 2 were performed at room temperature (RT), at a pore fluid pressure of 2.5 MPa. The other series were performed at 40 °C. Series 3 and the first measurements in series 4 were performed at a pore fluid pressure of 5.0 MPa. The later measurements in series 4 and series 5 were performed at a pore fluid pressure of 7.5 MPa. During each individual series of measurements, the sample was kept under pressure. However, between series, the sample was de-pressurized, either to replace the jacket or because of leakages of the confinement vessel. During a jacket replacement after the first series of measurements, the sample split along its bedding (parallel to the sample axis). Thus, series 2–5 were performed on a fractured sample.

All transient pulse permeabilities measured on Sample 2 are given in Table 2 and Fig. 4. Six series of measurements were performed, 1 and 2 at room temperature, using Ar and CO₂, respectively, then 3 to 6 at 40 °C, using, respectively, CO₂, Ar, water, and CO₂. Constant flow measurements were

performed during series 1 (Ar), 2 (CO₂), and 6 (CO₂). Constant flow permeabilities measured using argon (series 1) are given in Table 3. Note that during two of the last three of these measurements, the upstream pressure did not stabilize but kept decreasing slowly, while the downstream flowrate was stable, suggesting that the (apparent) permeability of the sample was increasing gradually. The permeabilities reported for these two measurements were calculated over a relatively stable portion of the pressure data, and should be considered high approximations. During constant flow tests using CO₂ (series 2 and 6), before a stable steady state could be achieved, sudden rapid flowthrough the sample occurred, causing the pressure differential across the sample to drop. An example of such a breakthrough event is shown in Fig. 5. As the figure shows, the upstream fluid pressure increased continuously with ongoing flow into the system, while initially, no flow was measured at the downstream side. Then, after about 30 min, minor flow was observed at the downstream side, while the upstream pressure continued to increase. After about 1 h, the maximum pore fluid pressure set on the pump was reached, and the upstream fluid pressure was kept constant by the pump, though with the maximum flowrate not exceeding that set previously. During this time, flow measured at the downstream side started to increase rapidly. This rapid increase in flow caused a strong drop in the upstream pressure to a value that was only slightly higher than the downstream pressure over a period of 25 min. A subsequent increase in pump flowrate caused only a very minor bump in upstream pressure, and a near-immediate increase in downstream flowrate.

Fig. 2 Graph showing pressure vs. time as measured during a typical transient pulse measurement. The measurement shown is 20160706 225CO240C3 (permeability $8.9 \times 10^{-18} \text{ m}^2$)

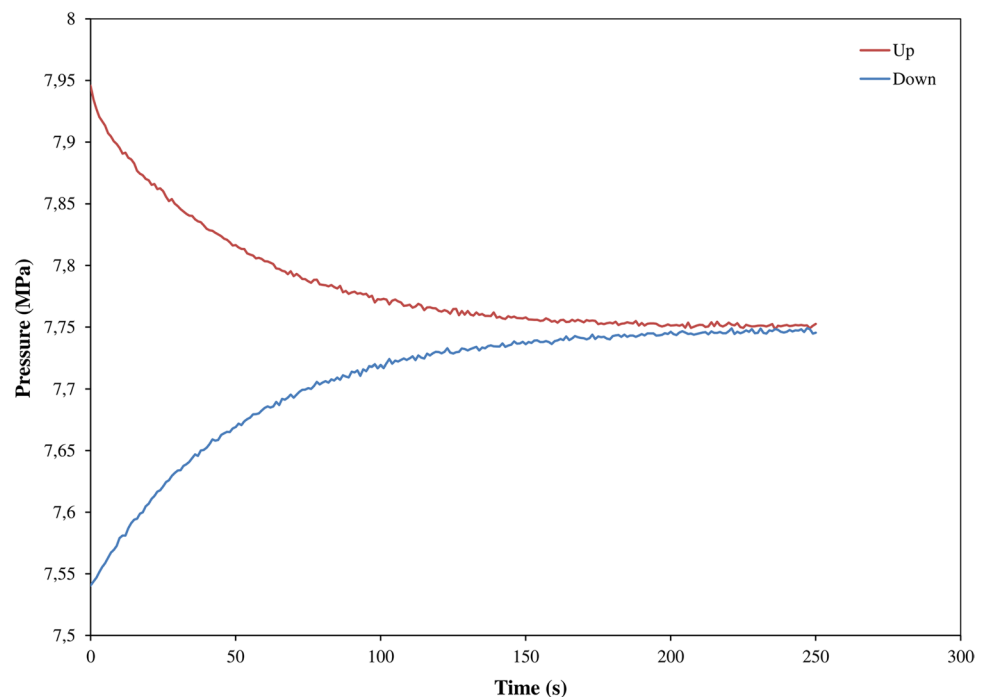


Table 1 All permeabilities (k) measured on Sample 1, and the conditions [background pore pressure (P_{pore}), pulse pressure step (P_{pulse}), effective confining pressure (P_{eff}) and temperature (T)] under which measurements were performed

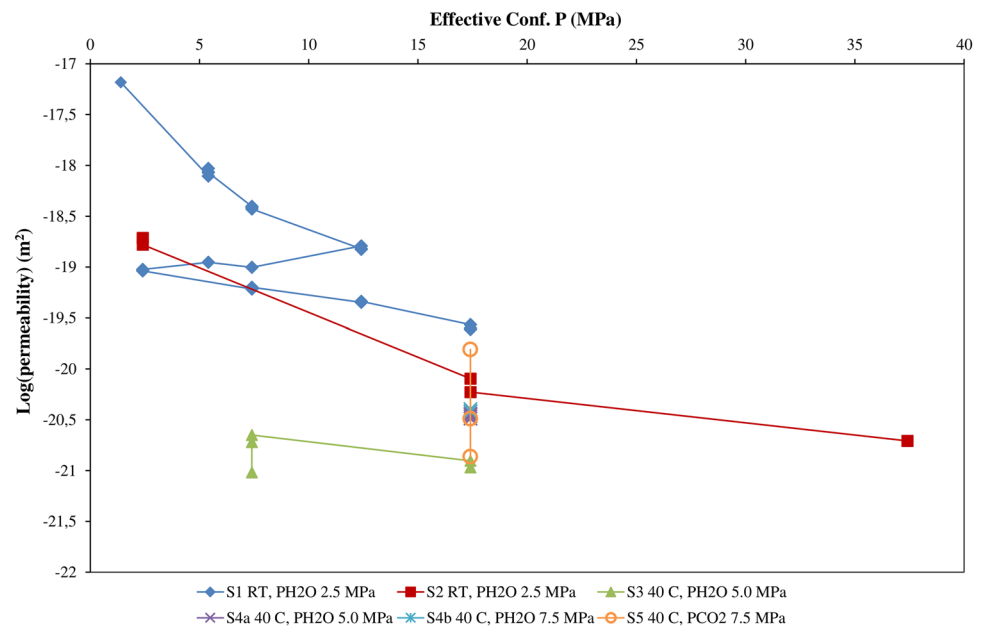
Measurement no.	Notes	P_{pore}	P_{pulse}	P_{eff}	T (°C)	k (m ²)	
1-40272501	Intact core, permeate water	2.5	0.2	1.4	RT	6.6×10^{-18}	
1-80272501		2.5	0.2	5.4	RT	7.9×10^{-19}	
1-80272502		2.5	0.2	5.4	RT	8.6×10^{-19}	
1-80272503		2.5	0.2	5.4	RT	9.3×10^{-19}	
1-80272504		2.5	0.2	5.4	RT	8.5×10^{-19}	
1-100272501		2.5	0.2	7.4	RT	3.9×10^{-19}	
1-100272502		2.5	0.2	7.4	RT	3.9×10^{-19}	
1-100272503		2.5	0.2	7.4	RT	3.7×10^{-19}	
1-1502725b03		2.5	0.2	12.4	RT	1.5×10^{-19}	
1-1502725b04		2.5	0.2	12.4	RT	1.5×10^{-19}	
1-1502725b05		2.5	0.2	12.4	RT	1.6×10^{-19}	
1-1002725b02		2.5	0.2	7.4	RT	9.9×10^{-20}	
1-802725c01		2.5	0.2	5.4	RT	1.1×10^{-19}	
1-502725c04		2.5	0.2	2.4	RT	9.5×10^{-20}	
1-502725c05		2.5	0.2	2.4	RT	9.2×10^{-20}	
1-1002725d01		2.5	0.2	7.4	RT	6.1×10^{-20}	
1-1002725d02		2.5	0.2	7.4	RT	6.3×10^{-20}	
1-1502725d01		2.5	0.2	12.4	RT	4.5×10^{-20}	
1-1502725d02		2.5	0.2	12.4	RT	4.6×10^{-20}	
1-2002725a01		2.5	0.2	17.4	RT	2.7×10^{-20}	
1-2002725b02	2.5	0.2	17.4	RT	2.5×10^{-20}		
1-2002725b03	2.5	0.2	17.4	RT	2.4×10^{-20}		
2-502725x01	Fractured core, permeate water	2.5	0.2	2.4	RT	1.9×10^{-19}	
2-502725x02		2.5	0.2	2.4	RT	1.9×10^{-19}	
2-502725x03		2.5	0.2	2.4	RT	1.7×10^{-19}	
2-2002725x01		2.5	0.2	17.4	RT	8.0×10^{-21}	
2-2002725x02		2.5	0.2	17.4	RT	5.9×10^{-21}	
2-4002725a01		2.5	0.2	37.4	RT	2.0×10^{-21}	
3-1255250x02		Fractured core, permeate water	5	0.2	7.4	40	1.9×10^{-21}
3-1255250x05			5	0.2	7.4	40	9.6×10^{-22}
3-1255250x06			5	0.2	7.4	40	2.2×10^{-21}
3-2255250 01			5	0.2	17.4	40	1.2×10^{-21}
3-2255250 02	5		0.2	17.4	40	1.1×10^{-21}	
4-2255250 e03	Fractured core, permeate water	5	0.2	17.4	40	3.6×10^{-21}	
4-2255250 e04		5	0.2	17.4	40	3.6×10^{-21}	
4-2255250 e05		5	0.2	17.4	40	3.8×10^{-21}	
4-2255250 e06		5	0.2	17.4	40	3.2×10^{-21}	
4-2255250 e07		5	0.2	17.4	40	3.4×10^{-21}	
4-2507775a01		7.5	0.2	17.4	40	3.8×10^{-21}	
4-2507775a02		7.5	0.2	17.4	40	4.0×10^{-21}	
5-2507775CO202	Fractured core, permeate scCO ₂	7.5	0.2	17.4	40	1.6×10^{-20}	
5-2507775CO203		7.5	0.2	17.4	40	3.2×10^{-21}	
5-2507775CO204		7.5	0.2	17.4	40	1.4×10^{-21}	

These measurements were previously reported in Van Noort and Yarushina (2016). All pressures are given in MPa

Transient pulse measurements carried out after flow measurements that resulted in an increase in permeability showed that the shale sample permeabilities quickly recovered to near-original values, but did remain slightly

elevated. Elevated permeabilities (relative to pre-break-through values) were still observed in transient pulse measurements carried out several days after the flow measurement.

Fig. 3 All permeability values measured on Sample 1, plotted against the effective confining pressure as (see also Van Noort and Yarushina 2016). The core split after the first series of measurements (between S1 and S2). The fourth measurement series (S4) was performed with two different pore fluid pressures (4a at 5.0 and 4b at 7.5 MPa)



In addition to pressure-dependent changes in permeability, time-dependent changes at constant pressure were also observed for some measurement series. Figure 6 shows time-dependent permeability changes at various confining pressures measured on Sample 1 (series 1) and Sample 2 (series 5). The main observations per measurement series are summarized in Table 4.

3.2 Klinkenberg Effect

In tight porous media, gas permeabilities can appear significantly higher than liquid permeabilities due to slip flow along pore walls, also known as the Klinkenberg effect (Klinkenberg 1941). The magnitude of this Klinkenberg effect is dependent on the mean pore radius (r), and on the mean free path of the gas molecules (λ). The latter in turn depends on the molecular diameter of the gas, and on temperature and pressure. The following equation was derived by Klinkenberg for the apparent gas permeability (k_g):

$$k_g = k_l \left(1 + \frac{4c\lambda}{r} \right). \quad (2)$$

In this equation, c is a constant with a value slightly smaller than 1, while k_l is the liquid (absolute) permeability. Following the approach used by Faulkner and Rutter (2000), we can calculate the ratio k_g/k_l . For argon (which has a molecular radius similar to that of CO₂), this suggests that for an assumed mean pore radius of 12 nm (cf. Faulkner and Rutter 2000; Katsube et al. 1991), the apparent gas permeability would be less than 1.3 times higher than the liquid permeability. For a very small mean pore radius (1 nm—Sakhaee-Pour and Bryant 2011), $k_g/k_l \approx 4$.

However, we can directly address the Klinkenberg effect in our samples by comparing our measurements made using CO₂ at room temperature (liquid) and at 40 °C (supercritical). Comparing these measurements, we observe a $\sim 1.2 \times$ increase in permeability for supercritical CO₂ relative to liquid CO₂. The magnitude of this difference is equivalent to the Klinkenberg effect for a mean pore radius of ~ 15 nm. In the following discussions, this small difference (comparable in magnitude to the difference between individual measurements) has been neglected.

3.3 Effect of Temperature

On both samples, permeability measurements were performed at room temperature (approximately 25 °C) and at 40 °C. The water permeability of shale recorded for Sample 1 did not show any changes that could clearly be ascribed to temperature effects, while for Sample 2, as discussed above, a direct comparison of the CO₂ permeability at room temperature and at 40 °C showed a minor increase in permeability with temperature. This effect most likely resulted from the CO₂-phase change from liquid to supercritical, suggesting that, at least in this limited temperature range, there was no direct effect of temperature for either sample.

3.4 Effect of Confinement

In all measurement series on both samples, we observed a decrease in permeability with increasing effective confining pressure. In the first series of measurements on Sample 1 (using water, at room temperature—see the blue line in Fig. 3 and all data in Fig. 6a), the permeability decreased by

Table 2 All permeabilities (k) measured on Sample 2, and the conditions [background pore pressure (P_{pore}), pulse pressure step (P_{pulse}), effective confining pressure (P_{eff}) and temperature (T)] under which measurements were performed

Measurement no.	Notes	P_{pore}	P_{pulse}	P_{eff}	T (°C)	k (m ²)
20160427 4 5	Permeate argon	7.5	0.2	4.9	RT	8.5×10^{-17}
20160427 6 7 8		7.5	0.5	4.75	RT	8.3×10^{-17}
20160429 1 2 5		7.5	0.2	7.4	RT	3.2×10^{-17}
20160429 3 4 6		7.5	0.5	7.25	RT	2.4×10^{-17}
20160510 1 2 5		7.5	0.2	7.4	RT	5.0×10^{-18}
20160510 3 4 6		7.5	0.5	7.25	RT	7.0×10^{-18}
20160520 1		7.5	0.2	9.9	RT	9.8×10^{-19}
20160520 2		7.5	0.2	9.9	RT	1.2×10^{-18}
20160520 4		7.5	0.5	9.75	RT	2.0×10^{-18}
20160520 5		7.5	0.5	9.75	RT	2.0×10^{-18}
20160520 8		7.5	0.5	9.75	RT	1.2×10^{-18}
20160520 9		7.5	0.5	9.75	RT	2.1×10^{-18}
20160525 1		7.5	0.2	14.9	RT	2.1×10^{-19}
20160525 2		7.5	0.2	14.9	RT	4.9×10^{-19}
20160602 3		7.5	0.5	14.75	RT	3.2×10^{-19}
20160602 4		7.5	0.5	14.75	RT	4.7×10^{-19}
20160602 5		7.5	0.2	14.9	RT	2.1×10^{-19}
20160602 6		7.5	1	14.5	RT	1.0×10^{-18}
20160602 7		7.5	0.5	14.75	RT	5.9×10^{-19}
20160602 8		7.5	0.2	14.9	RT	2.1×10^{-19}
20160602 9	7.5	0.5	14.75	RT	7.4×10^{-19}	
20160606 10	7.5	0.5	14.75	RT	4.7×10^{-19}	
20160606 11	7.5	0.5	14.75	RT	6.2×10^{-19}	
20160615 1b	7.5	0.5	7.25	RT	6.1×10^{-18}	
20160615 2b	7.5	0.5	7.25	RT	6.6×10^{-18}	
20160615 3b	7.5	0.2	7.4	RT	7.0×10^{-18}	
20160615 4b	7.5	0.2	7.4	RT	6.1×10^{-18}	
20160615 5b	7.5	0.5	7.25	RT	6.6×10^{-18}	
20160615 6b	7.5	0.2	7.4	RT	6.3×10^{-18}	
20160616 7b	7.5	0.5	7.25	RT	1.1×10^{-17}	
20160616 8b	7.5	0.5	7.25	RT	1.1×10^{-17}	
20160617 CO201	Permeate CO ₂	7.5	0.5	4.75	RT	3.5×10^{-17}
20160617 CO201		7.5	0.5	4.75	RT	3.5×10^{-17}
20160617 CO203		7.5	0.2	4.9	RT	3.5×10^{-17}
20160617 CO204		7.5	0.2	4.9	RT	3.3×10^{-17}
20160617 CO205		7.5	0.5	4.75	RT	3.5×10^{-17}
20160617 CO201		7.5	0.5	7.25	RT	2.0×10^{-17}
20160617 CO202		7.5	0.5	7.25	RT	1.9×10^{-17}
20160620 CO203		7.5	0.5	7.25	RT	1.2×10^{-17}
20160620 CO204		7.5	0.5	7.25	RT	1.1×10^{-17}
20160620 CO205		7.5	0.2	7.4	RT	1.2×10^{-17}
20160620 CO206 ^a		7.5	0.5	7.25	RT	1.1×10^{-17}
20160620 CO207 ^b		7.5	0.5	7.25	RT	3.3×10^{-16}
20160620 CO208 ^b		7.5	0.5	7.25	RT	1.1×10^{-16}
20160621 CO209 ^b		7.5	0.5	7.25	RT	3.3×10^{-17}
20160621 CO210 ^b		7.5	0.5	7.25	RT	3.1×10^{-17}
20160621 CO211 ^b		7.5	0.5	7.25	RT	3.1×10^{-17}
20160622 CO201 ^b		7.5	0.5	14.75	RT	1.8×10^{-17}
20160622 CO202 ^b		7.5	0.5	14.75	RT	1.8×10^{-17}
20160622 CO203 ^b		7.5	0.5	14.75	RT	1.7×10^{-17}
20160623 CO204 ^b		7.5	0.5	14.75	RT	1.5×10^{-17}

Table 2 (continued)

Measurement no.	Notes	P_{pore}	P_{pulse}	P_{eff}	T (°C)	k (m ²)
20160627 CO2b1		7.5	0.5	7.25	RT	1.2×10^{-17}
20160627 CO2b2		7.5	0.5	7.25	RT	1.5×10^{-17}
20160627 CO2b3		7.5	0.5	7.25	RT	1.3×10^{-17}
20160627 CO2b4		7.5	0.5	7.25	RT	1.5×10^{-17}
20160627 CO2b5		7.5	0.5	7.25	RT	1.4×10^{-17}
20160627 225CO2b1		7.5	0.5	14.75	RT	7.4×10^{-18}
20160628 225CO2b2		7.5	0.5	14.75	RT	7.4×10^{-18}
20160701 225CO2b6		7.5	0.5	14.75	RT	7.1×10^{-18}
20160704 225CO2b7		7.5	0.5	14.75	RT	8.1×10^{-18}
20160704 225CO2b8		7.5	0.5	14.75	RT	7.6×10^{-18}
20160704 225CO2b9		7.5	0.5	14.75	RT	8.4×10^{-18}
20160704 225CO2b6		7.5	0.5	7.25	RT	1.3×10^{-17}
20160704 146CO240C1	Permeate CO ₂	7.5	0.5	6.85	40	1.2×10^{-17}
20160705 150CO240C2		7.5	0.5	7.25	40	1.5×10^{-17}
20160705 150CO240C3		7.5	0.5	7.25	40	1.5×10^{-17}
20160705 150CO240C4		7.5	0.5	7.25	40	1.4×10^{-17}
20160705 150CO240C5		7.5	0.5	7.25	40	1.4×10^{-17}
20160705 225CO240C1		7.5	0.5	14.75	40	8.7×10^{-18}
20160705 225CO240C2		7.5	0.5	14.75	40	8.7×10^{-18}
20160706 225CO240C3		7.5	0.5	14.75	40	8.9×10^{-18}
20160706 225CO240C4		7.5	0.5	14.75	40	1.1×10^{-17}
20160712 150CO240Cb1		7.5	0.5	7.25	40	1.9×10^{-17}
20160713 150CO240Cb2		7.5	0.5	7.25	40	1.9×10^{-17}
20160713 150CO240Cb3		7.5	0.5	7.25	40	1.9×10^{-17}
20160713 150CO240Cb4		7.5	0.5	7.25	40	1.8×10^{-17}
20160714 150CO240Cb5		7.5	0.5	7.25	40	2.0×10^{-17}
20160718 125Ar40C03	Permeate argon	7.5	0.5	4.75	40	8.7×10^{-17}
20160719 150Ar40C03		7.5	0.5	7.25	40	5.0×10^{-17}
20160720 150Ar40C06		7.5	0.5	7.25	40	6.1×10^{-17}
20160721 150Ar40C07		7.5	0.5	7.25	40	5.1×10^{-17}
20160725 150Ar40C08		7.5	0.5	7.25	40	5.5×10^{-17}
20160725 150Ar40C09		7.5	0.5	7.25	40	4.8×10^{-17}
20160725 150Ar40C10		7.5	0.5	7.25	40	4.4×10^{-17}
20160725 225Ar40C01		7.5	0.5	14.75	40	2.3×10^{-17}
20160726 225Ar40C02		7.5	0.5	14.75	40	2.3×10^{-17}
20160726 225Ar40C03		7.5	0.5	14.75	40	2.4×10^{-17}
20160727 225Ar40C03		7.5	0.5	14.75	40	2.3×10^{-17}
20160727 225Ar40C03		7.5	0.5	14.75	40	2.3×10^{-17}
20160728 150Ar40Cb02		7.5	0.5	7.25	40	3.7×10^{-17}
20160728 150Ar40Cb03		7.5	0.5	7.25	40	3.2×10^{-17}
20160729 150Ar40Cb04		7.5	0.5	7.25	40	3.6×10^{-17}
20160729 150Ar40Cb05		7.5	0.5	7.25	40	3.5×10^{-17}
20160801 125H2O40C01	Permeate water	7.5	0.5	4.75	40	2.2×10^{-19}
20160801 125H2O40C02		7.5	0.5	4.75	40	2.3×10^{-19}
20160801 125H2O40C03		7.5	0.5	4.75	40	2.3×10^{-19}
20160801 150H2O40C01		7.5	0.5	7.25	40	1.8×10^{-19}
20160802 150H2O40C02		7.5	0.5	7.25	40	1.8×10^{-19}
20160802 150H2O40C03		7.5	0.5	7.25	40	1.8×10^{-19}
20160802 150H2O40C04		7.5	0.5	7.25	40	1.8×10^{-19}
20160803 150H2O40C05		7.5	0.5	7.25	40	1.7×10^{-19}
20160803 150H2O40C06		7.5	0.5	7.25	40	1.7×10^{-19}

Table 2 (continued)

Measurement no.	Notes	P_{pore}	P_{pulse}	P_{eff}	T (°C)	k (m ²)
20160804 225H2O40C01		7.5	0.5	14.75	40	7.2×10^{-20}
20160804 225H2O40C02		7.5	0.5	14.75	40	7.0×10^{-20}
20160805 225H2O40C03		7.5	0.5	14.75	40	6.8×10^{-20}
20160805 225H2O40C04		7.5	0.5	14.75	40	6.8×10^{-20}
20160808 225H2O40C05		7.5	0.5	14.75	40	5.3×10^{-20}
20160810 225H2O40C06		7.5	0.5	14.75	40	4.6×10^{-20}
20160810 225H2O40C07		7.5	0.5	14.75	40	4.6×10^{-20}
20160816 225H2O40C08		7.5	0.5	14.75	40	3.9×10^{-20}
20160817 225H2O40C10		7.5	0.5	14.75	40	3.9×10^{-20}
20160817 225H2O40C11		7.5	0.5	14.75	40	3.4×10^{-20}
20160818 150H2O40Cb01		7.5	0.5	7.25	40	3.8×10^{-20}
20160818 150H2O40Cb02		7.5	0.5	7.25	40	3.7×10^{-20}
20160819 150H2O40Cb03		7.5	0.5	7.25	40	3.8×10^{-20}
20160824 150H2O40Cb04		7.5	0.5	7.25	40	3.6×10^{-20}
20160826 125CO240Cx01	Permeate CO ₂	7.5	0.5	4.75	40	2.0×10^{-19}
20160829 125CO240Cx02		7.5	0.5	4.75	40	3.8×10^{-19}
20160831 125CO240Cx03		7.5	0.5	4.75	40	3.8×10^{-19}
20160901 125CO240Cx04 ^a		7.5	0.5	4.75	40	3.8×10^{-19}
20160901 145CO240Cy01 ^b		7.5	0.5	4.75	40	6.2×10^{-17}
20160902 125CO240Cy02 ^b		7.5	0.5	4.75	40	1.0×10^{-18}
20160912 150CO240Cy01 ^b		7.5	0.5	7.25	40	6.6×10^{-19}
20161013 150CO240Cy02 ^b		7.5	0.5	7.25	40	4.5×10^{-19}
20161013 150CO240Cy03 ^{a,b}		7.5	0.5	7.25	40	4.4×10^{-19}
20161013 150CO240Cz01 ^b		7.5	0.5	7.25	40	1.7×10^{-16}
20161013 150CO240Cz02 ^b		7.5	0.5	7.25	40	2.1×10^{-16}
20161013 150CO240Cz03 ^b		7.5	0.5	7.25	40	1.9×10^{-16}
20161017 150CO240Cz04 ^b		7.5	0.5	7.25	40	1.4×10^{-18}
20161017 150CO240Cz05 ^b		7.5	0.5	7.25	40	1.4×10^{-18}
20161025 150CO240Cz06 ^b		7.5	0.5	7.25	40	1.2×10^{-18}
20161025 150CO240Cz07 ^b		7.5	0.5	7.25	40	1.2×10^{-18}
20161028 150CO240Cz08		7.5	0.5	7.25	40	1.3×10^{-18}
20161028 150CO240Cz09		7.5	0.5	7.25	40	1.3×10^{-18}
20161031 150CO240Cz10		7.5	0.5	7.25	40	1.3×10^{-18}
20161031 150CO240Cz11		7.5	0.5	7.25	40	1.3×10^{-18}

All pressures are given in MPa

^aThe last measurement before one or more constant flow tests were performed

^bMeasurements influenced by previously performed constant flow tests

almost 2.5 orders of magnitude for an increase in P_{eff} from 1.4 to 17.4 MPa. In addition, when unloading from 12.4 to 2.4 MPa, the permeability decreased further, suggesting that the change in permeability was not only permanent, but also had a time-dependent component (i.e., creep). During series 2, after the sample had fractured, the sample permeability decreased by almost 2 orders of magnitude for an increase in P_{eff} from 2.4 to 37.4 MPa. Combining these two series, we observed a decrease in permeability in excess of 3.5 orders of magnitude for an increase in P_{eff} from 1.4 to 37.4 MPa. At $P_{\text{eff}} = 17.4$ MPa, the permeability of the split sample was lower than measured on the intact sample in series 1,

suggesting that the fracture through the sample had become sealed due to (time-dependent) compaction and that other microfractures in the sample had also sealed further (see also Van Noort and Yarushina 2016). However, at very low confining pressure (2.4 MPa), the permeability was higher than the last-measured value before fracturing, indicating that at this confining pressure, fracture flow may have resulted in an average sample permeability that was enhanced, though by less than 1 order of magnitude. When the sample was later removed from the holder (for another jacket replacement), the two halves adhered to one another, but did come loose easily. Finally, the CO₂-permeability measured on this

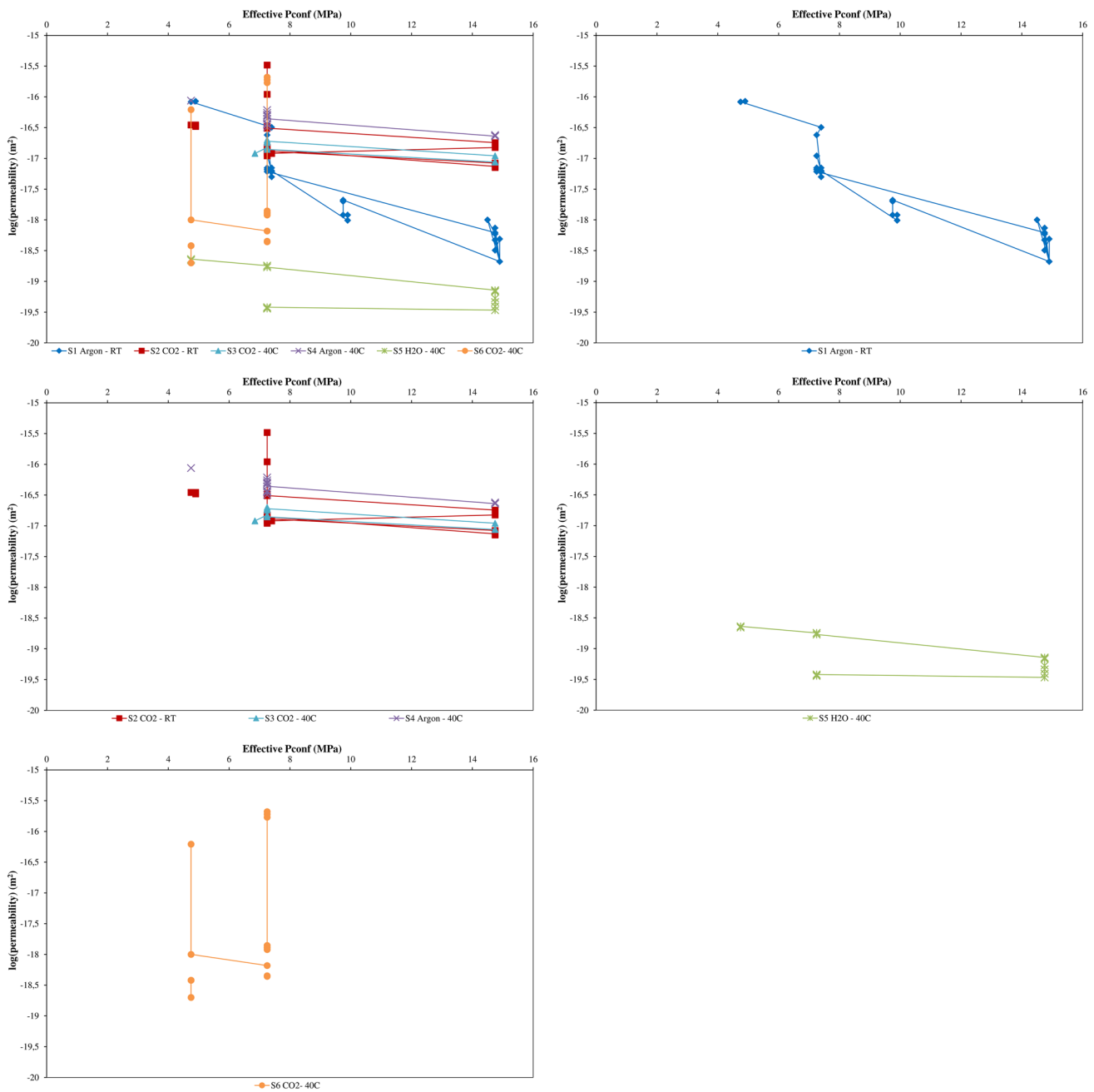


Fig. 4 All permeability values measured on Sample 2, plotted against the effective confining pressure. **a** All series of measurements combined; **b** series 1; **c** series 2–4; **d** series 5; **e** series 6

sample during series 5 showed a decrease by more than an order of magnitude over 26 days at constant pressure.

In the first series of measurements on Sample 2 (using Ar, at room temperature, see Fig. 4b), the permeability decreased by roughly 2.5 orders of magnitude when P_{eff} was increased from 4.9 to 14.9 MPa. Subsequently, during unloading from 14.8 to 7.3, the permeability increased by roughly an order of magnitude, back to similar values as observed during the loading stage. In the second series of

measurements (CO₂, RT), for the same increase in confining pressure, however, the permeability decreased by less than a factor 5, and similar smaller effects were subsequently observed in measurement series 3 and 4 (CO₂ or Ar, 40 °C).

Furthermore, during the first series of measurements on Sample 2 (Ar, RT), at $P_{eff} = 7.5$ MPa, we observed a time-dependent effect, with a decrease in permeability by almost a factor 5 after a period of 11 days (unfortunately no permeability measurements were performed during these 11 days).

Table 3 Constant flow permeability (k) measurements

	P_{conf}	P_{up}	P_{down}	P_{d}	T (°C)	Flow (ml/min)	k (m ²)	Notes
20160510a	16.3	7.36	7.17	0.19	26	0.2	8.2×10^{-18}	
20160510b	16.4	7.53	7.18	0.35	27	0.5	1.1×10^{-17}	
20160510c	16.5	7.83	7.19	0.64	27	1.0	1.3×10^{-17}	
20160510d	16.6	7.34	7.18	0.16	27	0.2	9.7×10^{-18}	
20160520a	18.6	7.2	6.95	0.25	25	0.2	6.1×10^{-18}	
20160520b	18.6	7.53	6.95	0.57	25	0.5	7.2×10^{-18}	
20160520c	18.7	7.17	6.95	0.21	25	0.2	7.2×10^{-18}	
20160602a	23.9	8.21	7.53	0.68	31	0.2	2.4×10^{-18}	
20160602b	23.9	7.81	7.5	0.31	31	0.1	2.5×10^{-18}	
20160606a	24.3	9.3	8.07	1.24	29	0.2	1.6×10^{-18}	Pup not stable
20160616a	15	7.89	7.63	0.26	24	0.2	5.2×10^{-18}	
20160616b	15	8.049	7.62	0.43	24	0.5	9.2×10^{-18}	Pup not stable

Confining pressure (P_{conf}), upstream pressure (P_{up}), downstream pressure (P_{down}), and differential pressure (P_{d}) are all given in MPa

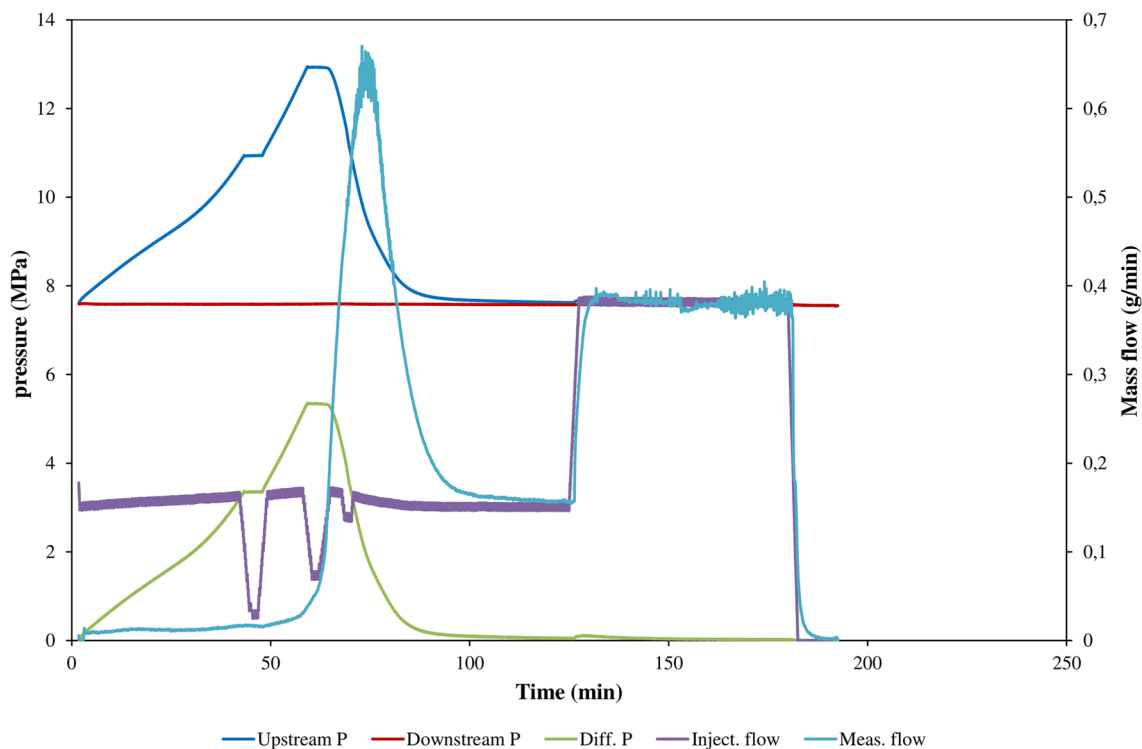


Fig. 5 Breakthrough of CO₂ during a flow-through permeability measurement. The upstream pressure increased up to a differential pressure of about 5.4 MPa and then remained stable at 5.3 MPa for about 3.2 min (due to reaching the pressure limit set on the pump), after which the differential pressure rapidly dropped to nearly zero. When the flowrate was increased (at roughly the 127 min mark), a

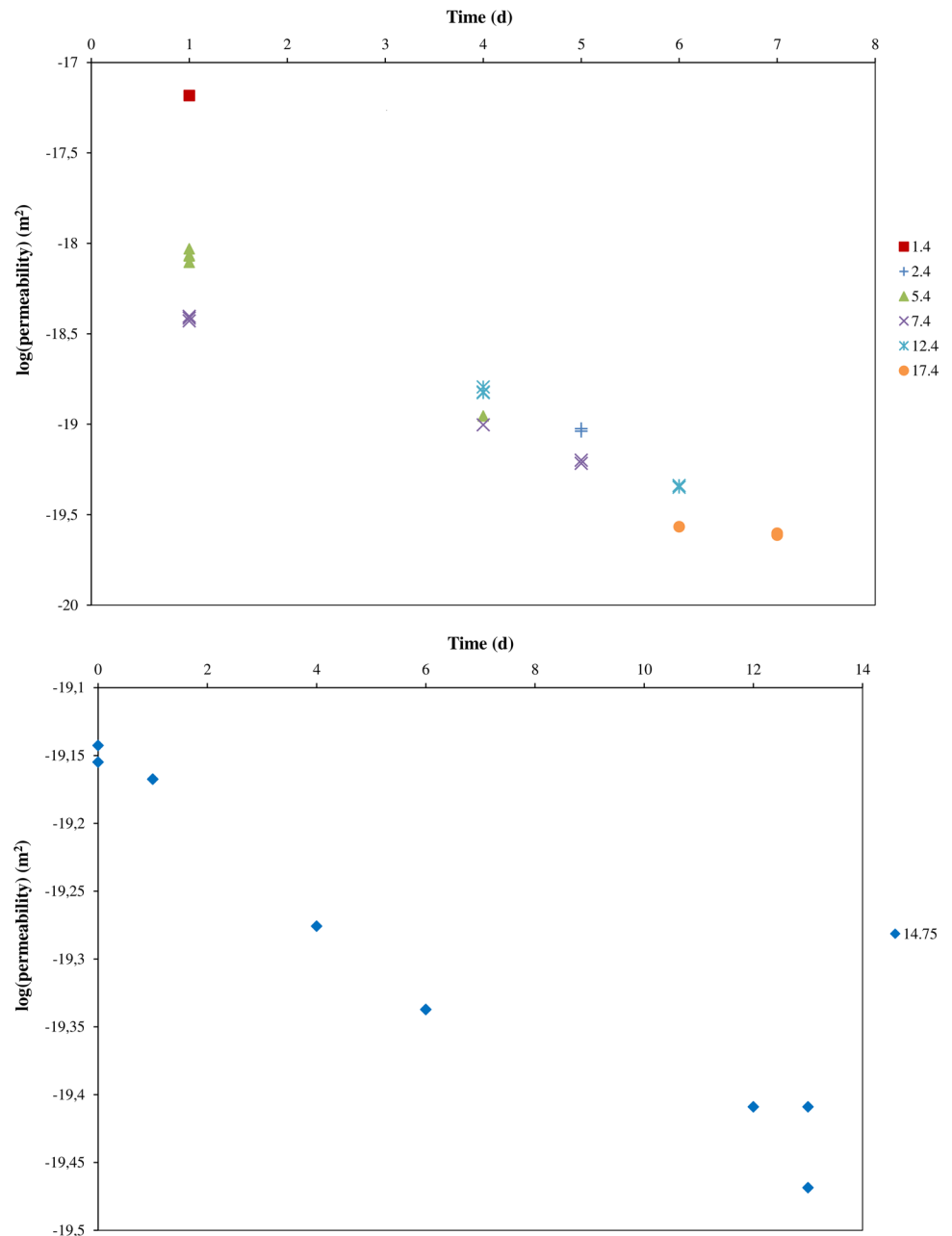
small increase in upstream (and hence differential) pressure was observed, which quickly dissipated. Note that the injection rate decreased some time before the breakthrough, because the upstream pressure reached the pressure limit set on the pump. The total confining pressure during this measurement was 15 MPa

A smaller time-dependent decrease in permeability was also observed during measurement series 5 (water, 40 °C), where the permeability decreased by about a factor 2 over 13 days at $P_{\text{eff}} = 15.0$ MPa (see Fig. 6b). During the other series of measurements on Sample 2, time-dependent effects were not

observed, except for the decreases in permeability observed after CO₂-flowthrough tests in which a breakthrough had occurred.

Finally, the decrease in permeability with increasing effective confining pressure observed in most measurement

Fig. 6 Time-dependent permeability changes. **a** Sample 1 series 1. Different symbols indicate different effective confining pressures. **b** Sample 2 series 5 (effective confining pressure 14.75 MPa)



series on Sample 2 was mainly reversible, as permeabilities returned to approximately their original values when the confining pressure was released. However, the time-dependent permeability decrease observed during the first series (at a confining pressure of 7.5 MPa) was not recovered. Furthermore, as for Sample 1, when water was used as the permeate, the permeability remained constant when the confining pressure was released. This suggests that pressure- and time-dependent permeability decreases in the presence of water were permanent, while permeability changes on relatively dry samples were mainly reversible in nature.

Based on the available data, the pressure dependence of shale permeability to Ar, CO₂, and water, and at 40 °C can

be quantified for Sample 2, assuming an exponential correlation of the form:

$$k \sim k_0 \exp(-\gamma (P_{\text{eff}} - P_0)). \quad (3)$$

Here, k_0 is the permeability at a reference effective pressure ($P_0 = 0$), and γ is a constant. For these substances, and an effective pressure ranging from 4.75 to 14.9 MPa, the values found for k_0 and γ are given in Table 5. Note that for Ar and CO₂, since these permeabilities returned to original values when the pressure was decreased, we used all data, not distinguishing between loading and unloading. As with water, a time-dependent permeability change was

Table 4 Overview of the measurement series performed, with the main observations per series

	Series #	Fluid	P_f (MPa)	T (°C)	Notable observations
Sample 1	1	Water	2.5	RT	Strong decrease in permeability with increasing pressure; not recovered during unloading; time-dependent permeability change
	2	Water	2.5	RT	Fractured sample; further decrease in permeability with increasing pressure
	3	Water	5.0	40	–
	4a	Water	5.0	40	–
	4b	Water	7.5	40	–
	5	CO ₂	7.5	40	Apparent CO ₂ -permeabilities measured similar to water permeabilities
Sample 2	1	Ar	7.5	RT	Relatively strong decrease in permeability with increasing confining pressure. Relatively low permeability (at higher confining pressure)
	2	CO ₂	7.5	RT	CO ₂ -breakthroughs observed in constant flow experiments
	3	CO ₂	7.5	40	–
	4	Ar	7.5	40	Ar permeability higher than CO ₂ -permeability (however, see Sect. 4.3)
	5	Water	7.5	40	Time-dependent permeability change. Permeability not recovered during unloading
	6	CO ₂	7.5	40	Relatively low permeability; CO ₂ -breakthroughs observed in constant flow experiments

Table 5 Values for k_0 [permeability at reference pressure ($P_0 = 0$)], and constant γ for argon, CO₂, and water and effective pressures ranging from 4.75 to 14.9 MPa

Substance	k_0 (m ²)	γ (MPa ⁻¹)
Argon	9.3×10^{-17}	0.042
CO ₂	2.8×10^{-17}	0.032
Water	4.1×10^{-19}	0.051

also observed at the highest effective pressure, we have only used measurements taken during the loading stage.

Similar exponential correlations between shale permeability and effective confining pressure were derived by Dong et al. (2010), Zhang et al. (2015, 2016a), and Al Ismail and Zoback (2016). The values derived here for γ compare well to the values reported by Dong et al. (2010) for the loading stage (0.017–0.043) on shale that had not been pre-compacted, but are higher than their values for the unloading stage (0.005–0.019). Zhang et al. (2015, 2016a) reported values for γ in the range 0.049–0.123; i.e., somewhat higher than reported here. Al Ismail and Zoback (2016) reported values for γ ranging from 0.049 to 0.132 (for layer-parallel flow) and 0.006 to 0.078 (for layer-perpendicular flow), measured on different lithologies. Furthermore, the values for k_0 obtained here fit in the range of values reported by Dong et al. (2010), but are somewhat higher than those reported by Al Ismail and Zoback (2016). However, as noted by (for example) Chalmers et al. (2012) and Ghanizadeh et al. (2014), mineralogy is an important factor controlling permeability and

the confining pressure dependence of shale permeability, which may explain the observed differences.

3.5 Effects of Water and Breakthroughs

The initial measurements performed on Sample 1 yielded CO₂ permeabilities that were comparable to its water permeabilities. The subsequent measurements on Sample 2, however, indicated that the quantity of water present in the pore network had a pronounced impact on sample permeability. The most pronounced effect was that the permeability of Sample 2 measured using water as the permeate was 2.0–2.5 orders of magnitude lower than the permeability measured using (dry) CO₂ or Ar. Furthermore, in the presence of water (Sample 1 and measurements series 5 and 6 on Sample 2), decreases in permeability with increasing confining pressure and with time appeared permanent, whereas without water permeabilities recovered to initial values when the confining pressure was released (i.e., changes were elastic).

An additional effect of the presence of water in the pore network is observed when comparing the first series of measurements performed on Sample 2 (RT, Ar) to the following series of measurements on the same sample. Prior to the first measurements, the shale samples had been stored under moist conditions. Therefore, when the first series of measurements (Ar) was performed, the shale pore network contained an unknown quantity of hydrous pore fluid. During this first series, a strong decrease in permeability with increasing confining pressure was observed, as well as a time-dependent decrease in permeability at a constant effective confining pressure of 7.5 MPa. Subsequent series of measurements, using CO₂ or Ar, at RT or 40 °C, showed a much less pronounced decrease in permeability with increasing confining pressure, resulting in higher permeabilities

than measured before at higher confining pressures. The main differences between this first series and later series of measurements are that during the first measurement series micro-damage due to sample treatment was still present in the sample, and the sample contained a larger amount of water in the pore network as water was increasingly displaced or removed by the dry Ar and dry CO₂. While sealing of the micro-damage could explain a stronger confining pressure dependence of permeability, it does not explain the lower permeabilities measured during the first measurement series. However, the subsequent removal of hydrous pore fluid from the pore network during permeate changes can explain this observation.

During the last series of measurements, performed on Sample 2 and using CO₂ after a series of measurements had been performed using water, an initial permeability was observed that was similar to the (relatively low) water permeabilities at the same P_{eff} , just as had been observed for the CO₂ permeability of Sample 1. This could indicate that saturating our shale samples with water and confining them had caused a permanent permeability change. However, during subsequent flow-through measurements on Sample 2, sudden increases in permeability were observed, leading to breakthroughs of CO₂. Once flow was stopped, the permeability increases induced during such breakthroughs largely disappeared quickly, over a timespan of minutes, but somewhat elevated permeabilities were still measured in transient pulse tests days afterwards. The same breakthrough events were also observed during flow-through tests performed using CO₂ at room temperature (during measurement series 2), but such sudden breakthroughs were not observed when using Ar (measurement series 1).

4 Discussion

4.1 Presence of Water

The results presented above show that the presence of water, either as the permeating fluid or as a residual phase trapped in the pore network, can have significant impacts on the permeability of a shale rock and its dependence on stress and loading history, even during the flow of other fluids. There are two main mechanisms through which the presence of hydrous fluids may have caused the observed permeability effects. First, water may affect the microstructure of the shale itself, by enhancing plastic deformation and/or creep, and inducing the swelling of clays. Second, the presence of water in the pore network may affect the accessibility of this pore network to other fluids through surface adsorption and/or capillary effects, for example, leading to a pore-size-dependent capillary entry pressure that has to be overcome for a non-wetting fluid to enter pores filled with a wetting

fluid (e.g., Skurtveit et al. 2012; Rozhko 2016 and references therein). We will now discuss how our observations can be explained by these effects.

During the first series of measurements on Sample 2, using Ar, we observed a stronger dependence of permeability on confining pressure, and lower permeabilities at higher confining pressure, compared to later series using Ar or CO₂. The initial strong decrease in permeability observed at lower confining pressures likely resulted from sealing of damage induced during sample preparation. However, this cannot explain the lower permeabilities measured during this first series at higher confining pressures compared to subsequent measurements using Ar or CO₂. During the first series of measurements on Sample 2, this sample was moist as it had been stored under moist conditions. After the first series, the replacement of Ar with CO₂, and subsequently the replacement of CO₂ with argon again, likely resulted in the removal of part of this pore water, resulting in a drier sample. This could suggest that increased compaction in the moist sample resulted in a stronger dependence of permeability on confining pressure. However, while the measurements performed with water as the permeate (Sample 2, series 5) give lower permeabilities, the permeability/stress-correlation coefficient is comparable to that of the assumed-dry measurements. If the shale was indeed mechanically weakened by the presence of water, then a significantly stronger decrease in permeability with increasing confining pressure would have been expected in these measurements as well. Thus, water did not directly enhance pressure-dependent (elastoplastic) deformation of the sample. Instead, the lower permeabilities measured at higher confining pressure must be ascribed to an inhibition of flow due to the presence of a hydrous pore fluid blocking transport pathways such as pore throats and narrow fractures. As the confining pressure was elevated, the squeezing of the pore network, both decreasing its volume and reducing pore (throat) width, would then have resulted in an increase in the fraction of the pore volume filled with water. As this water blocks the flow of non-wetting fluids, this enhances the inhibiting effect that a small amount of water present in the pore network can have on flow, resulting in a lower effective permeability. After the first series of measurements reported here, this free water had mostly been removed from the pore network, thus reducing the effect of water on the stress dependence of apparent permeability. The lower CO₂ permeabilities measured on Sample 2 in measurement series 6 compared to the earlier measurements using CO₂ or Ar can then be ascribed to a significantly higher sample water content following the water-permeability measurements performed during series 5. The relatively low CO₂ permeabilities measured on Sample 1 were also measured after permeability measurements using water,

and are likewise explained by the sample's relatively high water content as a result of its prior saturation. Similarly, Ghanizadeh et al. (2014) reported that the gas permeability of a "as-received" shale, containing less than 2% wt. moisture, was up to two times lower than the permeability of the same shale dried, which they ascribed to the inhibition of gas flow by water adsorbed at pore throats.

When considering the permeability measured using water as the permeate, one possible explanation for the lower permeability compared to values measured using Ar or CO₂ is the swelling of smectite in the shale in the presence of water (cf. Ilton et al. 2012; Schaef et al. 2012; De Jong et al. 2014). However, since the sample contained only minor smectite (as an interlayer phase with illite), it is not likely that swelling had a significant effect. Instead, one possible explanation for the lower permeability to water is the inhibition of flow through narrow throats due to the presence of structured water films on mineral surfaces. Ghanizadeh et al. (2014) reported a shale permeability to water that was up to three orders of magnitude lower than the permeability of the same shale to gas (Ar or CH₄), which they ascribed to either structured water films that inhibited the flow of pore water, or enhanced compaction in the presence of water. An alternative explanation for the lower permeability to water than to CO₂ or Ar can be found in the model of Rozhko (2016), which suggests that relative permeabilities of crack-like pores may be influenced not only by pore fluid pressure, but also by surface tension and rock wettability, resulting in a lower permeability for wetting fluids, such as water, relative to non-wetting fluids, such as CO₂. Based on the data available, it is not possible to distinguish whether structured water films or fluid-dependent pore shape effects were the main flow inhibiting mechanism in our samples.

In addition, during the measurement series using water as the permeate (on both samples), the permeability did not increase when the confining pressure decreased. This may be explained by the formation of adsorbed water films on mineral surfaces and the short range attractive forces (van der Waals forces—cf. Vigil et al. 1994) between mineral surfaces at very small separation in the presence of water. When the confining pressure is increased, mineral surfaces are brought closer together due to elastic compaction, and when the spacing between the surfaces becomes sufficiently small, these surfaces become attracted to one another (Vigil et al. 1994). Subsequently, when the confining pressure is decreased, the attractive forces between the surfaces may overcome the elastic relaxation of the shale microstructure, keeping the surfaces adhered to each other, connected through a thin adsorbed water film, and as a result, the flow inhibition caused by pore closure at higher pressures is maintained at lower pressure.

Finally, during the first series (Ar, but moist) and fifth series (water) of permeability measurements on Sample 2, time-dependent changes in permeability were observed (see Fig. 6b) that were not recovered upon unloading. These changes are ascribed to compaction creep, which is enabled when sufficient water is present (cf. Sone and Zoback 2014).

4.2 CO₂ Breakthrough Events

The presence of water may likewise explain the CO₂-breakthrough events observed during constant flow measurements on Sample 2, during series 2 and 6 (Fig. 5, see also Sect. 3.1). When water is present, this results in a capillary entry pressure as CO₂ (a non-wetting fluid) needs to displace water (a wetting fluid) to enter the narrow pore network. The breakthrough effects observed here, however, cannot be fully explained by a simple, single capillary entry pressure, as some flow was already observed on the downstream side of our sample before breakthrough took place. One possible explanation for this effect, then, is a bimodal pore-size distribution (e.g., see Zhang et al. 2016b). As the capillary entry pressure is dependent on the pore aperture (e.g., Rozhko 2016), a bimodal pore-size distribution can result in two different entry pressures. Initial flow through the sample started when the entry pressure for one part of the pore network was overcome, as also occurred during the pulse measurements. At the higher upstream pressures occurring during the constant flow measurements, the higher entry pressure for narrower pore throats and microfractures was also overcome, removing the inhibition to flow to a larger part of the pore network, and leading to the observed sudden increases in permeability (see also Hildenbrand et al. 2002, 2004). After flow has been halted, during subsequent recovery or when the confining pressure is increased, water migrated from larger pores (to where it had been displaced) back into narrower pore throats and microcracks, driven by surface energy effects (capillary forces), causing the permeability to decrease again.

An alternative mechanism is presented by, for example, Skurtveit et al. (2012), who combined measurements of the breakthrough pressure of CO₂ in wet shales with in-situ measurements of sample deformation. They observed sample dilatation before a breakthrough event, and, based on post-experiment CT scanning, interpreted this as the opening of a (pre-existing) fracture creating a single pathway for fluid flow. Considering that in our experiments, the confining pressure was always at least 2 MPa higher than the fluid pressure, actual hydrofracturing (which requires a pore fluid pressure in excess of the confining pressure) was not likely to occur (see also Hildenbrand et al. 2002, 2004). However, increases in pore fluid pressure may result in dilatation through elastic relaxation as the effective confining pressure decreases. As suggested by the model of Rozhko

(2016), injection of a non-wetting fluid (e.g., CO₂) into a pore network containing a wetting fluid (e.g., water) may result in pore deformation and dilatation induced by capillary effects. This can then result in a sudden sharp enhancement of permeability. Based on the results obtained here, it is not possible to determine whether in our experiments, permeability enhancement was localized (for example, along a single vertical fracture) or pervasive throughout the pore–crack network.

After each breakthrough, a semi-permanent increase in permeability was observed. Once flow is stopped, the permeability initially recovers very rapidly, decreasing by up to half an order of magnitude in only minutes, but then remains elevated by about half an order of magnitude relative to the pre-breakthrough permeability. As the pore fluid pressure already decreased during, and as a result of, the breakthrough, any (elastic) compaction already took place at that time, and therefore, this recovery cannot be explained by fluid migration into the pore throats caused by elastic compaction (squeezing) of the pore network. A more likely explanation then is that the flow of water from larger pores into pore throats was driven by surface energy or capillary effects. Likewise, if the breakthroughs observed were caused by a dilatation of the pore network due to changes in the stress state, it would be expected that as soon as the injection pressure drops (due to enhanced flowthrough the sample), compaction results in a decrease in permeability (cf. Skurtveit et al. 2012), leading to a new build-up of injection pressure. Since this was not observed, this suggests that the breakthrough effect is related to capillary or surface energy effects rather than to dilation of the pore–fracture network resulting from changes in pore fluid pressure.

During most constant flow measurements using Ar, a stable P_{UP} was achieved, and no change in permeability was observed, except during two of the Ar measurements, where the upstream pressure decreased gradually at constant flow, implying that the permeability was slowly increasing. However, a sudden breakthrough as seen in the CO₂ measurements was not observed in the Ar measurements performed. This suggests that Ar was less successful at displacing water than CO₂. This could be related to differences in the water–argon and water–CO₂ surface tensions, but further measurements are required to confirm this observation and investigate it in more detail.

There is an interesting similarity between the breakthrough effect observed here, and the solitary porosity waves (e.g., Revil 2002; Cai and Bercovici 2013; Räss et al. 2014; Yarushina et al. 2015), which arise as a result to an obstruction to fluid flow, and may be formed in elastic, viscous, or viscoplastic rocks with non-linear pressure-dependent permeability. Such porosity waves lead to a (temporary) enhancement of permeability induced by local changes in fluid pressure (and thus effective confining pressure). They

represent elongated cylindrical channels with size strongly dependent on the viscosity and permeability of the rock as well as fluid viscosity, though their shape may also be controlled by rock anisotropy. They have self-sealing properties, and the channel is formed largely due to dilatation of existing pores, so that after propagation of the channel, there would be no sign of a fracture. A proper understanding of these breakthrough effects and porosity waves is required to properly assess the integrity of any CO₂-storage reservoir over which shale forms the caprock.

4.3 Argon and CO₂ Permeabilities

We have already discussed the permeabilities measured using CO₂ at room temperature (series 2), and at 40 °C (series 3), and explained the ~1.2 times higher permeability at 40 °C in terms of the Klinkenberg effect. The permeabilities measured at 40 °C using Ar are about half an order of magnitude higher than the CO₂ permeabilities. This difference was most likely caused by a decrease in the sample moisture content, induced during pore fluid replacements (see also Ghanizadeh et al. 2014). Alternatively, CO₂ may adsorb on clay surfaces, potentially causing this clay to swell (Ilton et al. 2012; Schaef et al. 2012; De Jong et al. 2014), causing a reduction in permeability (cf. Pini et al. 2009). A similar effect was reported by Al Ismail et al. (2014), who reported a 10% decrease in layer-parallel shale permeability and a much larger, ~1 order of magnitude reduction in layer-perpendicular permeability, ascribed to CO₂ adsorption. However, since in our samples, the content of phases that may swell (smectite, organics) was minor, this is less likely to have been significant.

4.4 Comparison of Samples 1 and 2

Based on the measurements on Sample 1, in Van Noort and Yarushina (2016), we reported the following observations:

- Shale permeability decreased with increasing effective confining pressure.
- Permeability did not recover during subsequent unloading, suggesting permanent deformation.
- Permeability change also had a time-dependent component, interpreted as a result of compaction creep.
- At elevated confining pressure (17.4 MPa), a bedding-parallel fracture through our sample no longer influenced permeability, and even gained minor cohesion.
- No significant difference between water- and CO₂-permeability was observed.

Here, these observations will be addressed in view of our additional results.

All our measurements support the observation that shale permeability decreases with increasing confining pressure, as has also been reported in the literature (e.g., Dong et al. 2010; Chalmers et al. 2012; Ghanizadeh et al. 2014; Heller et al. 2014; Zhang et al. 2015, 2016a). However, while this decrease appeared to be permanent when water was the pore fluid, with CO₂ or Ar as the pore fluid the permeability increases again when the confining pressure is released. As discussed above, the apparently permanent decrease in permeability with increasing confining pressure when water is the pore fluid may have resulted from water film formation on mineral surfaces, and attraction forces between mineral surfaces in the presence of water. When other fluids are the pore fluid, such effects do not occur, and thus, permeabilities return to (near-)original values when the pressure is released. Dong et al. (2010) report only a partial recovery of the permeability when the stress on a silty shale is released. However, they did not perform a second pressure cycle to distinguish between the effects related to the sealing of damage to the sample induced during sample preparation, and actual elastic pressure effects on a sample in which damage had been sealed.

Time-dependent permeability changes were observed on both samples when using water as the permeate, and during the first series of measurements on Sample 2 (using Ar as a permeate, but with some moisture present in the sample). The time-dependent effect observed on Sample 2 when using Ar may in part have been related to sealing of the (micro-) damage induced in the shale during sample preparation. However, most likely all observed time-dependent permeability changes resulted from creep compaction enabled in the presence of water (cf. Sone and Zoback 2014).

While no significant difference between the water and the CO₂ permeability was observed on Sample 1, on Sample 2, we observed a difference of up to 2.8 orders of magnitude between its water permeability, and its Ar or CO₂ permeability. This is in agreement with the observations of Ghanizadeh et al. (2014). Furthermore, in accordance with Ghanizadeh et al. (2014), the moisture content of the shale samples measured here strongly impacted its permeability to other fluids (Ar, CO₂, etc.). This strong control of water content on permeability indicates that it is important to measure shale permeabilities containing realistic, in-situ moisture contents. Furthermore, it suggests that the desiccation of samples before measurements can potentially have a significant impact on stress-dependent shale permeability. The low CO₂-permeability measured on Sample 1, comparable to its water permeability, was most likely the result of a high sample water content, since measurements using water as the permeate were performed first.

Finally, based on the above discussions, as the permeability of a shale is strongly influenced by its water content, the most direct comparison of the permeabilities

of Samples 1 and 2 can be obtained by comparing the measurements made on each sample using water as the permeate. In doing so, it should be remembered that for water measurements the permeability does not recover upon unloading. Figure 7 shows the first series of measurements on Sample 1 and the water-permeability measurements performed on Sample 2 (series 5). The lower permeability of Sample 2 at low confining pressure is due to the fact that the sample had already been compacted previously. Hence, any microcracks and similar damage resulting from sample preparation had already been sealed. At somewhat higher confining pressure, where the effects of micro-damage can be neglected, the P_{eff} -dependent permeability of Sample 2 overlaps with that of Sample 1, indicating good agreement in permeabilities between these two samples.

5 Conclusions and Implications

Based on 180 transient pulse permeability measurement and 12 constant flow measurements, on two shale core plugs from the same lithology, using Ar, CO₂ or water, we report the following observations:

- Shale permeability decreases with increasing effective confining pressure.
- Shale has a lower permeability to water than to other fluids (Ar and CO₂), most likely due to the inhibition of flow by structured water layers on mineral surfaces, or due to surface tension effects (e.g., Rozhko 2016). A potential effect of clay swelling was not likely in our samples, but cannot be excluded.
- Small quantities of water present in the pore network, localized at pore throats and narrow fractures, will inhibit the flow of other fluids (such as Ar or CO₂), leading to a lower (apparent) permeability.
- If a sufficient, constant flow of CO₂ is applied to a sample containing a hydrous pore fluid, the resulting increase in injection pressure leads to a breakthrough once a pore-size-dependent capillary entry pressure is overcome. Possible mechanisms leading to this breakthrough are the displacement of water or dilation, and further work would be required to determine which mechanism, if not both, was active. After such a breakthrough, once the CO₂ flow is stopped, the elevated permeability mostly recovers to lower values in minutes, but some permeability enhancement may remain.
- When water is the pore fluid, the decrease in permeability when the confining pressure is elevated is not recovered when the confining pressure is released. A possible cause for this may be attractive forces between

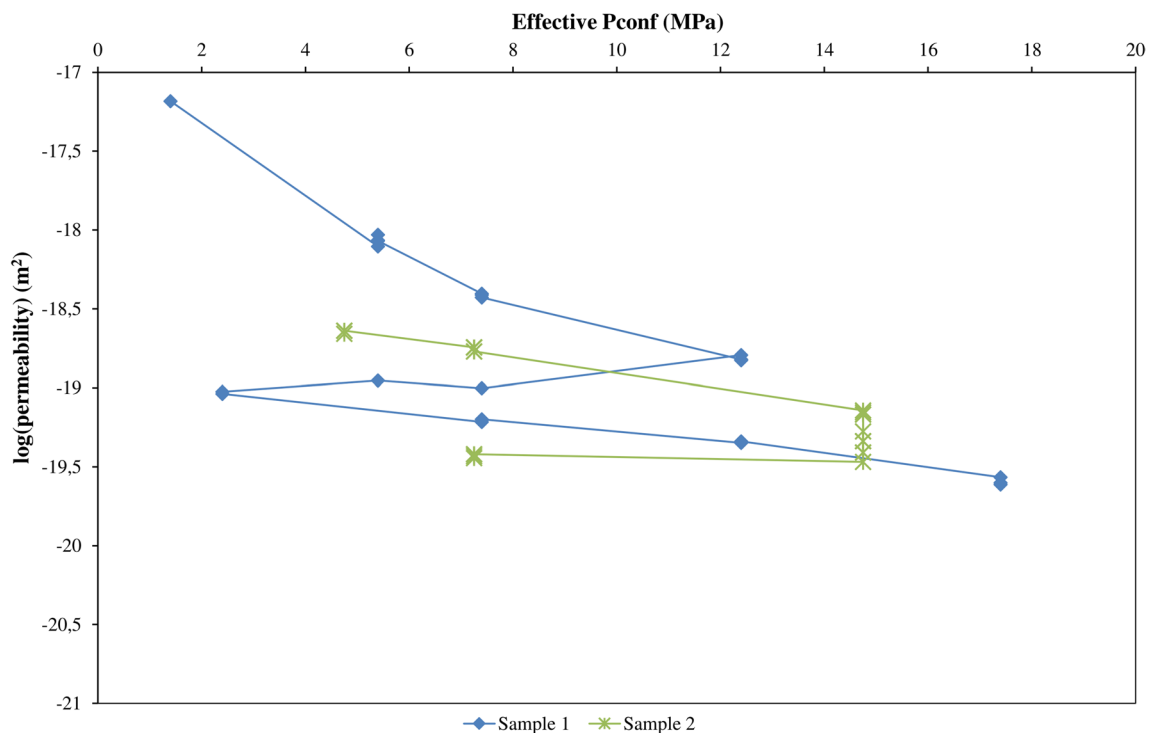


Fig. 7 Comparison of the first series of permeability values measured on Sample 1 (RT) and the fifth series of permeability values measured on Sample 2 (40 °C), both using water as permeate. The permeabilities are plotted against the effective confining pressure. The relatively high permeability at low confining pressure measured on

Sample 1 (relative to those measured on Sample 2) are ascribed to micro-damage of the sample induced during sample preparation, that was no longer present in Sample 2 as this sample had already been confined prior to the measurements shown

mineral surfaces that have been brought close together under the high confining pressure.

- Under confinement and in the presence of sufficient water, compaction creep can occur, causing a further, permanent decrease in permeability.

Our results suggest that shale permeability can be influenced by pressure-dependent and time-dependent deformation. This implies that for the long-term safety of CO₂ storage, shale caprocks need to be characterized thoroughly with respect to their deformation properties and the impact of caprock deformation on shale permeability.

Based on our observations, we further conclude that the water content of a shale caprock is of key importance in controlling its permeability to other fluids, such as CO₂, and thus its integrity as a seal during long-term exposure. The exact mechanisms by which water may affect permeability, in particular its roles in inhibiting flow and during breakthrough events, have not been fully determined. This is important, since our results suggest that, independently of swelling clay content, drying may strongly impact the effective permeability of shale to CO₂ (and other fluids). While such drying is unlikely to have a strong effect on the

integrity of sufficiently thick layers of unfractured shale, the flow of dry CO₂ along leakage pathways such as well-bores or fractures could induce drying, and contribute to shale permeability along these pathways. When characterizing shale as a caprock, the effects of water content should be thoroughly considered.

One potential direction for future work towards addressing the above issues may be through measurements conducted on analogue samples with well-controlled mineral composition and water content. The strong pressure dependence of shale permeability, the effect of pore water content, and shale's non-linear rheology have significant consequences for hydraulic fracturing of unconventional reservoirs as well as for understanding the role of shales as a seal in sub-surface waste storage (Yarushina et al. 2013).

Acknowledgements This work was funded by the Research Council of Norway (Grants 193825/S60 and 280953). The authors wish to acknowledge Alexander Rozhko for his useful contributions in interpreting our observations, and the two anonymous reviewers whose helpful comments improved the quality of our paper.

Open Access This article is distributed under the terms of the Creative Commons Attribution 4.0 International License (<http://creativecommons.org/licenses/by/4.0/>)

[mmons.org/licenses/by/4.0/](https://creativecommons.org/licenses/by/4.0/)), which permits unrestricted use, distribution, and reproduction in any medium, provided you give appropriate credit to the original author(s) and the source, provide a link to the Creative Commons license, and indicate if changes were made.

References

- Al Ismail MI, Zoback MD (2016) Effects of rock mineralogy and pore structure on stress-dependent permeability of shale samples. *Phil Trans R Soc A* 374:20150428. <https://doi.org/10.1098/rsta.2015.0428>
- Al Ismail MI, Hol S, Reece JS, Zoback MD (2014) The effect of CO₂ adsorption on permeability anisotropy in the eagle ford shale. In: Society of Petroleum Engineers (SPE), unconventional resources technology conference, Denver, Colorado, USA. SPE paper URTeC 1921520
- Alemu BL, Aagaard P, Munz IA, Skurtveit E (2011) Caprock interaction with CO₂: a laboratory study of reactivity of shale with supercritical CO₂ and brine. *Appl Geochem* 26:1975–1989
- Armitage PJ, Faulkner DR, Worden RH (2013) Caprock corrosion. *Nat Geosci* 6:79–80
- Bateman K, Rochelle CA, Purser G, Kemp SJ, Wagner D (2013) Geochemical interactions between CO₂ and minerals within the Utsira caprock: a 5-year experimental study. *Energy Procedia* 37:5307–5314
- Borchardt JK, Roll DL, Rayne LM (1984) Use of a mineral fines stabilizer in well completions. In: SPE California regional meeting. Society of Petroleum Engineers
- Borysenko A, Clennell B, Sedev R, Burgar I, Ralston J, Raven M, Dewhurst D, Liu K (2009) Experimental investigations of the wettability of clays and shales. *J Geophys Res* 114:B07202. <https://doi.org/10.1029/2008JB005928>
- Braathen A, Bælum K, Christiansen HH, Dahl T, Eiken O, Elvebakk H, Hansen F, Hanssen TH, Jochmann M, Johansen TA, Johnsen H, Larsen L, Lie T, Mertes J, Mørk A, Mørk MB, Nemeč W, Olaussen S, Oye V, Rød K, Titlestad GO, Tveranger J, Vagle K (2012) The Longyearbyen CO₂ Lab of Svalbard, Norway—initial assessment of the geological conditions for CO₂ sequestration. *Norw J Geol* 92:353–376
- Brantut N, Heap MJ, Meredith PG, Baud P (2013) Time-dependent cracking and brittle creep in crustal rocks: a review. *J Struct Geol* 52:17–43
- Busch A, Bertier P, Gensterblum Y, Rother G, Spiers CJ, Zhang M, Wentinck HM (2016) On sorption and swelling of CO₂ in clays. *Geomech Geophys Geoenergy Georesour* 2:111–130. <https://doi.org/10.1007/s40948-016-0024-4>
- Cai ZY, Bercovici D (2013) Two-phase damage models of magma-fracturing. *Earth Planet Sc Lett* 368:1–8
- Chalmers GRL, Bustin RM (2012) Geological evaluation of Halfway–Doig–Montney hybrid gas shale-tight gas reservoir, northeastern British Columbia. *Mar Petrol Geol* 38:53–72
- Chalmers GRL, Ross DJK, Bustin RM (2012) Geological controls on matrix permeability of Devonian Gas Shales in the Horn River and Liard basins, northeastern British Columbia, Canada. *Int J Coal Geol* 103:120–131
- Chang CD, Zoback MD (2009) Viscous creep in room-dried unconsolidated Gulf of Mexico shale (I): Experimental results. *J Pet Sci Eng* 69:239–246
- Chhatre SS, Braun EM, Sinha S, Determan MD, Passey QR, Zirkle TE, Wood AC, Boros JA, Berry DW, Leonardi SA, Kudva RA (2014) Steady state stress dependent permeability measurements of tight oil bearing rocks. In: International symposium of the Society of Core Analysts, Avignon, France, 8–11 Sept 2014
- Creodoz A, Bildstein O, Jullien M, Raynal J, Pétronin JC, Lillo M, Pozo C, Geniaut G (2009) Experimental and modeling study of geochemical reactivity between clayey caprocks and CO₂ in geological storage conditions. *Energy Procedia* 1:3445–3452
- De Jong SM, Spiers CJ, Busch A (2014) Development of swelling strain in smectite clays through exposure to carbon dioxide. *Int J Greenh Gas Control* 24:149–161
- Delage P, Cui YJ, Tang AM (2010) Clays in radioactive waste disposal. *J Rock Mech Geotech Eng* 2:111–123
- Dong J-J, Hsu J-Y, Wu W-J, Shimamoto T, Hung J-H, Yeh E-C, Wu Y-H, Sone H (2010) Stress-dependence of the permeability and porosity of sandstone and shale from TCDP Hole-A. *Int J Rock Mech Min* 47:1141–1157
- Faulkner DR, Rutter EH (2000) Comparisons of water and argon permeability in natural clay-bearing fault gouge under high pressure at 20 °C. *J Geophys Res* 105:B7:16415–16426
- Ghanizadeh A, Amann-Hildenbrand A, Gasparik M, Gensterblum Y, Krooss BM, Littke R (2014) Experimental study of fluid transport processes in the matrix system of the European organic-rich shales: II. Posidonia Shale (Lower Toarcian, northern Germany). *Int J Coal Geol* 123:20–33
- Ghanizadeh A, Bhowmik S, Haeri-Ardakani O, Sanei H, Clarkson CR (2015) A comparison of shale permeability coefficients derived using multiple non-steady-state measurement techniques: examples from the Duvernay Formation, Alberta (Canada). *Fuel* 140:371–387
- Gutierrez M, Oino LE, Nygard R (2000) Stress-dependent permeability of a de-mineralised fracture in shale. *Mar Petrol Geol* 17:895–907
- Gutierrez M, Katsuki D, Tutuncu A (2015) Determination of the continuous stress-dependent permeability, compressibility and poroelasticity of shale. *Mar Petrol Geol* 68:614–628
- Harrington JF, Milodowski AE, Graham CC, Rushton JC, Cuss RJ (2012) Evidence for gas-induced pathways in clay using a nanoparticle injection technique. *Mineral Mag* 76:3327–3336
- Heller R, Vermynen J, Zoback M (2014) Experimental investigation of matrix permeability of gas shales. *AAPG Bull* 98:975–995
- Hildenbrand A, Schlömer S, Krooss BM (2002) Gas breakthrough experiments on fine-grained sedimentary rocks. *Geofluids* 2:3–23
- Hildenbrand A, Schlömer S, Krooss BM, Littke R (2004) Gas breakthrough experiments on pelitic rocks: comparative study with N₂, CO₂ and CH₄. *Geofluids* 4:61–80
- Huq F, Smalley PC, Mørkved PT, Johansen I, Yarushina V, Johansen H (2017) The Longyearbyen CO₂ lab: fluid communication in reservoir and caprock. *Int J Greenh Gas Con* 63:59–76
- Ilton ES, Schaefer HT, Qafoku O, Rosso KM, Felmy AR (2012) In situ X-ray diffraction study of Na⁺ saturated montmorillonite exposed to variably wet super critical CO₂. *Environ Sci Technol* 46:4241–4248
- Katsube TJ, Mudford BS, Best ME (1991) Petrophysical characteristics of shales from the Scotian shelf. *Geophys* 56:1681–1689
- Klinkenberg LJ (1941) The permeability of porous media to liquids and gases. *SOCAR Proc* 2:200–213
- Makhnenko RY, Vilarrasa V, Mylnikova D, Laloui L (2017) Hydro-mechanical aspects of CO₂ breakthrough into clay-rich caprock. *Energy Procedia* 114:3219–3228
- Pini R, Ottiger S, Burlini L, Storti G, Mazzotti M (2009) Role of adsorption and swelling on the dynamics of gas injection in coal. *J Geophys Res* 114:B04203. <https://doi.org/10.1029/2008JB005961>
- Räss L, Yarushina VM, Simon NSC, Podladchikov YY (2014) Chimneys, channels, pathway flow or water conducting features—an explanation from numerical modelling and implications for CO₂ storage. *Energy Procedia* 63:3761–3774

- Räss L, Makhnenko RY, Podladchikov YY, Laloui L (2017) Quantification of viscous creep influence on storage capacity of caprock. *Energy Procedia* 114:3237–3246
- Revil A (2002) Genesis of mud volcanoes in sedimentary basins: A solitary wave-based mechanism. *Geophys Res Lett.* <https://doi.org/10.1029/2001GL014465>
- Rozhko AY (2016) Two-phase fluid-flow modeling in a dilatant crack-like pathway. *J Pet Sci Eng* 146:1158–1172
- Sakhaee-Pour A, Bryant S (2011) Gas permeability of shale. In: Society of Petroleum Engineers (SPE), annual technical conference and exhibition, Denver, Colorado, USA. SPE paper 146944
- Schaefer HT, Ilton ES, Qafoku O, Martin PF, Felmy AR, Rosso KM (2012) In situ XRD study of Ca²⁺ saturated montmorillonite (STX-1) exposed to anhydrous and wet supercritical carbon dioxide. *Int J Greenh Gas Control* 6:220–229
- Skurtveit E, Aker E, Soldal M, Angeli M, Wang Z (2012) Experimental investigation of CO₂ breakthrough and flow mechanisms in shale. *Pet Geosci* 18:3–15
- Sone H, Zoback MD (2014) Time-dependent deformation of shale gas reservoir rocks and its long-term effect on the in situ state of stress. *Int J Rock Mech Min* 69:120–132
- Tian S, Ren W, Li G, Yang R, Wang T (2017) A theoretical analysis of pore size distribution effects on shale apparent permeability. *Geofluids.* <https://doi.org/10.1155/2017/7492328> (article ID 7492328)
- Van Noort R, Yarushina VM (2016) Water and CO₂ permeability of a shale sample core from Svalbard. *Energy Procedia* 97:67–74
- Vigil G, Xu Z, Steinberg S, Israelachvili JN (1994) Interactions of silica surfaces. *J Colloid Interface Sci* 165:367–385
- Wagner W (2014) FLUIDCAL, software for the calculation of thermodynamic and transport properties of a great number of fluids. Ruhr-Universität Bochum, Bochum
- Wiseall AC, Cuss RJ, Graham CC, Harrington JF (2015) The visualization of flow paths in experimental studies of clay-rich materials. *Mineral Mag* 79:1335–1342
- Yarushina VM, Podladchikov YY (2015) (De)compaction of porous viscoelastoplastic media: model formulation. *J Geophys Res Sol Earth.* <https://doi.org/10.1002/2014JB011258>
- Yarushina VM, Bercovici D, Oristaglio ML (2013) Rock deformation models and fluid leak-off in hydraulic fracturing. *Geophys J Int* 194:1514–1526
- Yarushina VM, Podladchikov YY, Connolly JAD (2015) (De)compaction of porous viscoelastoplastic media: solitary porosity waves. *J Geophys Res Sol Earth.* <https://doi.org/10.1002/2014JB011260>
- Zhang R, Ning Z, Yang F, Wang X, Zhao H, Wang Q (2015) Impacts of nanopore structure and elastic properties on stress-dependent permeability of gas shales. *J Nat Gas Sci Eng* 26:1663–1672
- Zhang R, Ning Z, Yang F, Zhao H, Wang Q (2016a) A laboratory study of the porosity-permeability relationships of shale and sandstone under effective stress. *Int J Rock Mech Min* 8:19–27
- Zhang Y, Shao D, Yan J, Jia X, Li Y, Yu P, Zhang T (2016b) The pore size distribution and its relationship with shale gas capacity in organic-rich mudstone of Wufeng-Longmaxi Formations, Sichuan Basin, China. *J Nat Gas Geosci* 1:213–220

Publisher's Note Springer Nature remains neutral with regard to jurisdictional claims in published maps and institutional affiliations.